Materials and Design 60 (2014) 72–84

Contents lists available at ScienceDirect

Materials and Design

journal homepage: www.elsevier.com/locate/matdes

Technical Report

Residual stress induced by cold spray coating of magnesium AZ31B extrusion

G. Shayegan [a], H. Mahmoudi [a], R. Ghelichi [b,1], J. Villafuerte [c], J. Wang [c], M. Guagliano [b], H. Jahed [a,*]

[a] Mechanical and Mechatronics Engineering Department, University of Waterloo, Waterloo, Canada
[b] Department of Mechanical Engineering, Politecnico di Milano, Via G. la Masa, 1, Milan, Italy
[c] CenterLine Windsor Ltd, Windsor, Canada

ARTICLE INFO

Article history:
Received 27 December 2013
Accepted 22 March 2014
Available online 3 April 2014

ABSTRACT

Aluminum particles were successfully sprayed on wrought magnesium AZ31B extrusion using the cold spray technology. Cold spray high impact velocity of particles colliding with the substrate induced beneficial compressive residual stresses. Magnitude of the residual stress at the surface and its distribution through the thickness were measured using X-ray diffraction. With particle spraying velocity of 400 m/s, the residual stress was measured to be −25 MPa at the surface. The process of collision and development of residual stress was then modeled using LS-DYNA software to study the effect of the cold spray process parameters on the residual stress profile. Various models were employed to simulate the impact of the single and multiple particles. An asymmetric material model that considers the strain rate effect was employed to model AZ31B different behavior in tension and compression. Results of simulations for impact of multiple particles were compared with the results of XRD measurements on the substrate surface and through the depth of the substrate. After the validation of the models, a parametric study was performed on the impact of a single particle to find the optimum cold spray particle velocity, size, shape, incident angle, and friction parameters. Parameters leading to the optimum residual stress profile are introduced herein.

© 2014 Elsevier Ltd. All rights reserved.

1. Introduction

The economic and environmental benefits of increased fuel economy and reduced emissions are constantly driving the transportation sector to reduce the vehicles weight. In this regard, light metals such as Magnesium alloys due to high specific strength are attractive candidates for vehicle parts [1–3]. However, due to low creep and corrosion resistance the percentage of magnesium alloys used in transportation vehicles has traditionally been low. Increasingly demanding applications in automotive and aerospace have driven the development of magnesium corrosion-protective coatings. Cold spray coating is one of the protective methods that can be employed for this purpose. Cold spray is an emerging, solid-state spraying process in which the coating materials are not melted in the spray gun [4]; instead, the kinetic energy of supersonically accelerated solid particles is converted into interfacial heat upon impact with the substrate. This produces a combination of mechanical and metallurgical bonding. Corrosion protection by cold spray is promising to address many of the shortcomings associated with classical methods for corrosion protection of magnesium alloys. However, more research is required to understand and optimize the cold spray process [5]. Most of the recent studies on cold spray have focused on bonding mechanism and critical velocity. Residual stresses can contribute to fatigue life enhancement [6] but only few works have studied the residual stress induced by cold spray.

Price et al. [7] studied the effect of the deposition of titanium on titanium. Coatings were performed on as-received and grit-blasted samples. Rotating bending fatigue test of samples before and after coating revealed a 15% reduction in fatigue endurance limit of the as-received samples, but no significant reduction was observed on the grit-blasted substrate. The reduction in the fatigue endurance limit was attributed to the residual stress induced by the coating. However, in a different study, Cizek et al. [8] considered the cold spray of titanium on Ti6Al4V substrates. The average fatigue lives of cold sprayed samples were reduced by 9% as compared to the as-received specimens. Luzin et al. [9] studied the residual stress in Cu and Al coated samples by neutron powder diffraction stress measurement. They used the Tsui and Clyne's progressive model [10] that was originally developed to model the residual stress

* Corresponding author. Address: 200 University Avenue West, Waterloo, Ontario N2L5H5, Canada. Tel.: +1 5198884567x37826.
E-mail address: hjahed@uwaterloo.ca (H. Jahed).
[1] Present address: Department of Mechanical Engineering, Massachusetts Institute of Technology, 77 Mass Ave, Cambridge, MA, USA.

http://dx.doi.org/10.1016/j.matdes.2014.03.054
0261-3069/© 2014 Elsevier Ltd. All rights reserved.

Nomenclature

A	Johnson–Cook parameter (MPa)
a	major radius of ellipse (μm)
B	Johnson–Cook parameter (MPa)
b	minor radius of ellipse (μm)
C	Johnson–Cook parameter
C_0	bulk speed of sound (m/s)
D	strain rate parameter
d	first order volume correction to γ_0
d_p	penetration depth (μm)
d_b	depth of maximum compressive residual stress (μm)
d_{rtmax}	depth of maximum tensile residual stress(μm)
E	internal energy per unit volume (N/m^2)
m	Johnson–Cook parameter
n	Johnson–Cook parameter
P	pressure (MPa)
p	strain rate parameter
S_1, S_2, S_3	coefficients of the slope of the $U_s - U_p$ curve
T	instantaneous temperature (K)
T_{room}	room temperature (K)
T_{melt}	melt temperature (K)
U_s	shock wave velocity (m/s)
Up	particle velocity (m/s)
σ	Von Mises stress (MPa)
σ_0	quasi-static yield stress (MPa)
σ_y	flow stress (MPa)
σ_{rcmax}	maximum compressive residual stress (MPa)
σ_{rs}	surface residual stress (MPa)
σ_{rtmax}	maximum tensile residual stress (MPa)
$\dot{\varepsilon}$	strain rate (s^{-1})
$\bar{\varepsilon}^p$	effective plastic strain
$\dot{\bar{\varepsilon}}^p$	effective plastic strain rate (s^{-1})
$\dot{\varepsilon}_0^p$	effective plastic strain rate at quasi-static threshold (s^{-1})
γ_0	Gruneisen's gamma at the reference state
ρ	current density (g/cm^3)
ρ_0	initial density(g/cm^3)

accumulation in thermal spray coatings, to interpret their empirical results. Luzin et al. [9] concluded that the residual stress is determined almost entirely by the plastic deformation process of the spray material, due to the high velocity impact of the particles. Spencer et al. [11] also followed the same approach using Tsui and Clyne's progressive model [10] to understand the residual stress induced by cold spraying Al and Al alloy on Mg substrates. The residual stress distribution in their work was obtained by measurements using neutron diffraction. They concluded that the residual stress profile was more dependent on the alloy content, i.e. intrinsic resistance to plastic deformation, than the spray processing conditions. Sansoucy et al. [12] studied the cold spray of Al–13Co–26Ce alloy particles on AA 2024-T3 substrate. The results showed that the Al–Co–Ce coatings improved the fatigue behavior of AA 2024-T3 specimens when compared to uncoated specimens. They attributed the increase in the fatigue properties to the residual compressive stresses induced in the coatings. Jeong and Ha [13] investigated the effect of cold spraying aluminum alloy A356 powder on the substrate made of the same material. They reported a significant 200% improvement in the fatigue strength of the coated samples. The effect of cold spray coating on microstructure, residual stresses distribution and fatigue life of Al5052 substrate coated with pure aluminum and Al7075 powders was studied by Ghelichi et al. [14]. They reported a 30% increase in fatigue life of coated samples as compared to the as-received, when tested under the cantilever fully reversed bending test. The increase in life was attributed to the presence of the residual stress after the cold spray. Moridi et al. [15] studied the effect of cold spray of Al6082 by the same material on its fatigue life. They showed that the fatigue strength of coated samples was increased by 15%.

Modeling the cold spray process has also been of interest to many researchers. Assadi et al. [16] simulated the impact of single particle and substrate by an axisymmetric model with ABAQUS/Explicit. They concluded that the bonding of particles can be attributed to adiabatic shear instabilities, which occur at the particle/substrate or particle/particle interfaces, at high velocities. They also suggested that density and particle temperature are two main parameters determining the critical velocity. Grujicic et al. [17] analyzed the cold gas dynamic spray (CGDS) process by numerical modeling of the impact between a single spherical feed-powder particle and a semi-infinite substrate. They have investigated two cases of deposition of copper particles on aluminum and aluminum particles on copper. Experimental results show more efficient deposition of copper particles on aluminum. Their simulation has related this to higher density of copper particles, which causes higher kinetic energy, higher pressure at the contact area and larger interfacial area. Li et al. [18] considered the deformation behavior of Al particles upon impact on the Al substrate by using the Arbitrary Lagrangian Eulerian (ALE) method, available in LS-DYNA to clarify the deposition characteristics of Al powder and the effect of surface oxide film in the cold spray process. They applied the Johnson–Cook plasticity model as the material model for particles and substrate, and the Johnson–Holmquist plasticity damage model for oxide film (Al_2O_3). They concluded that the deformation behavior of Al particles is different from that of the Cu particles under the same impact conditions, which is attributed to the lower density of Al and thus less kinetic energy upon impact. They found Al particles need higher velocity to reach the same compression ratio as that of the Cu particles. Also, by increasing the impact velocity, the compression ratios of Al particles increase linearly. Kumar et al. [19] deposited smooth spherical and irregular granular copper powders on copper and aluminum substrates through the kinetic spray deposition process in order to find the effect of the feedstock powder state on the deformation process and the deposition behavior. Simulation for two kinds of powders was performed through ABAQUS explicit finite element analysis using a dynamic explicit procedure. They concluded that the coatings produced from irregular granular powder have higher bonding properties due to higher frictional dissipation effects. Li et al. [20] simulated three-dimensional modeling of particle impacting behavior in cold spraying by using ABAQUS/Explicit for copper and other materials. They examined various combinations of calculation settings concerning material damage, Arbitrary Lagrangian Eulerian adaptive meshing, distortion control, and contact interaction. They concluded that, by being given the appropriate material properties, the simulation can estimate critical velocity for the particle deposition. Li et al. [21] owing to the asymmetric characteristic of the oblique impacting, employed 3D models using LS-DYNA. They found that in the oblique impact the additional tangential component of the particle velocity along the substrate surface could create a tensile force and decrease the total contact area and bonding strength between the particle and the substrate. Ghelichi et al. [22] developed a numerical model of the cold spray process aimed to calculate the critical velocity. They used ABAQUS Explicit in order to simulate a 3D full model of particle impact on the substrate with Lagrangian formulation. They showed that their

results represent a very good correspondence with the experimental measurements of Raletz et al. [23]. Yin et al. [24] used LS-DYNA finite element software to examine the deformation behavior of the oxide film on an Al 6061-T6 particle surface after cold spray coating. They simulated particles and substrates by using the Johnson–Cook plasticity model and used the Johnson–Holmquist plasticity damage model to characterize the oxide film (Al_2O_3) deformation. They concluded that the oxide film can be disrupted during the high velocity impact and found that substrate hardness, particle velocity and spray angle all influenced the deformation behavior and final state of the oxide film. Xie et al. [25] investigated the particle deformation behavior in the cold spray process by using ABAQUS. They presented the simulation results of multiple impacts to estimate the porosity rate and residual stress induced by the cold spray within the coating and the substrate. Yin et al. [26] considered the effects of total pressure and nozzle divergent length on the flow characteristics and particle speed during the cold spray coating process. Using a 2D axisymmetric model, they employed the computational fluid dynamic (CFD) method and performed numerical simulations using ANSYS-FLUENT, to calculate particle speed and the gas flow regime in cold spray. The results show that the total pressure and divergent length have a considerable effect on flow regime and particle acceleration. Ghelichi et al. [27] investigated the residual stress evolution in the cold spray coating process through experiments and numerical simulations. They simulated the cold spray coating process for two material substrates, Al5052 and Al6061, coated by Al7075 via a 3D model in ABAQUS/Explicit. They calculated the stresses induced during the cold spray process and then took into account the annealing effect through an analytical model. They observed the significant effect of annealing on the eventual stress distribution in the cold sprayed substrate.

In this study, Al1100 powder has successfully been cold spray coated on magnesium AZ31B extrusion. The effect of cold spray coating in creating residual stress on the substrate is studied. X-ray diffraction was used to quantify the magnitude and distribution of residual stress induced by the cold spray process. Using LS-DYNA, a numerical model is developed to simulate the formation of residual stress in the cold spray. The anisotropy of AZ31B, due to different deformation mechanisms in tension and compression, has been taken into account. The impact of single and multiple particles on substrate made of AZ31B has been simulated and the induced residual stresses have been determined and compared with experimental results. The results obtained from numerical simulation are compared with experimental results. A parametric study is then performed and the influence of parameters on residual stress profiles has been investigated. Parameters yielding an optimum distribution of residual stress are discussed.

2. Cold spray coating process

In a cold spray coating process, mixtures of pure metals, metal alloys, metal–ceramic, metal–polymer particles are accelerated to supersonic speeds and propelled against a metal, polymeric, or ceramic substrate to produce a combined metallurgical and mechanical bonded deposit at low temperatures. In order to accelerate particles, a carrier gas (N_2, He or Air) is heated, and then accelerated through a converging–diverging DeLaval nozzle to supersonic velocities. Particles are then injected into the supersonic gas jet downstream or upstream the nozzle throat. The likelihood of the formation of a cold sprayed coating depends on the particle velocity as, at a given particle temperature, every material has a minimum critical velocity (V_{cr}) for bonding to the substrate. Bonding to the substrate is induced by sufficient plastic deformation of regions at the particle interface upon collision with the substrate at velocities above the critical velocity of the material. Fig. 1 illustrates a downstream injection cold spray system used in this research.

The impact of the cold spray particle on the substrate surface creates localized plastic deformation. Fig. 2 illustrates the plasticity induced near the surface of a magnesium substrate coated with aluminum particles, which is bounded in a large elastic zone. In result of this near surface permanent deformation and the surrounding elastic boundaries, residual stresses are created by the impact and are maintained after adhesion. The self-balanced residual stresses tend to occur as compressive stresses at the surface and tensile stresses below the surface, and then diminish away from the surface.

3. Materials and tests

The material used in the present study is the magnesium alloy AZ31B extrusion. The air-quenched section of the AZ31B extrusion was manufactured by Timminco. This section was extruded from a billet, which was 177.8 mm in diameter, 406.4 mm in length and had an extrusion ratio of 6. The extrusion temperature was between 360 °C and 382 °C, and the extrusion exit speed was 50.8 mm/s. The composition of the alloy is presented in Table 1 [29].

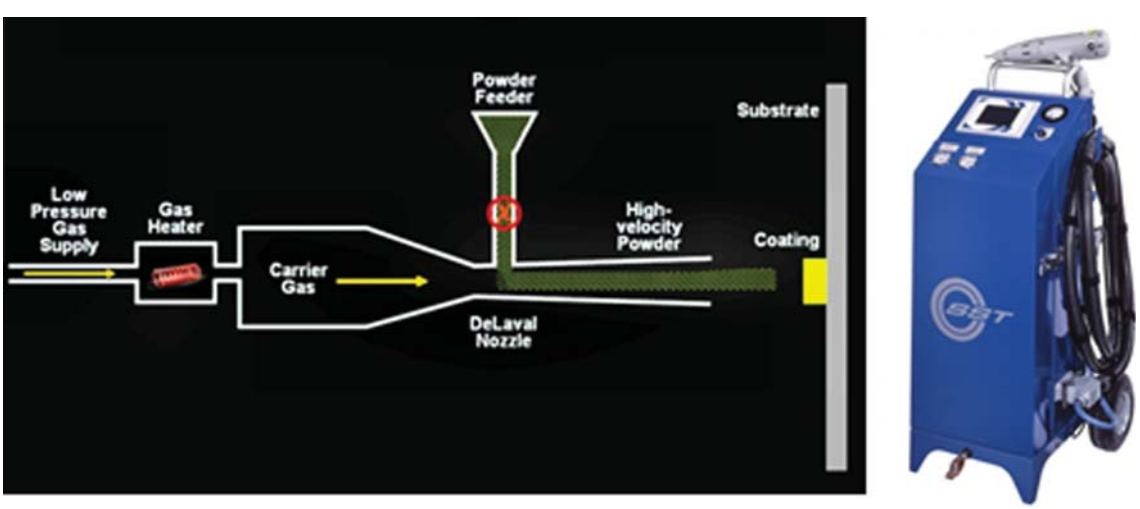

Fig. 1. Downstream injection cold spray apparatus [28].

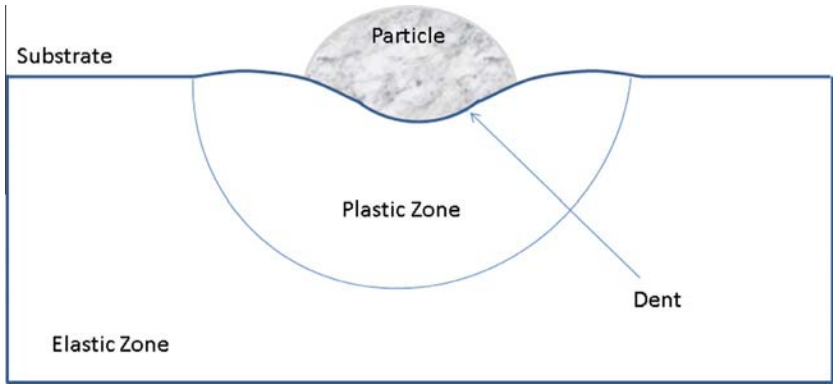

Fig. 2. High impact of Al particles induces local plasticity around contact surface on the Mg substrate.

Table 1
Chemical composition for extruded AZ31B (wt.%) [29].

Al	Mn	Zn	Fe	Ni	Cu
3.10	0.54	1.05	0.0035	0.0007	0.0008

Magnesium has a hexagonal closed-packed (HCP) crystal structure. Magnesium alloys present a tension–compression asymmetry. With limited slip systems for Mg alloys, deformation twining plays a major role in wrought magnesium deformation. While basal slip causes the yielding in tension, loading in compression along extrusion direction causes the activation of extension twins along the *c*-axis. The different deformation mechanisms in tension and compression result in different yield strength and post yield hardening behavior in AZ31B [30]. Fig. 3 shows the behavior of AZ31B extrusion in tension and compression.

Flat samples were machined from the extrusion piece. There was an initial compressive residual stress in as-received specimens due to the extrusion process. The first step was to apply a stress relief process to relieve the initial residual stress. For stress relief, the ASM recommended method was employed [31]. This standard recommends a thermal process of 260 °C for 15 min. To verify the stress relief process, residual stress on the surface of as-received and stress-relieved samples was measured. Table 2 provides the stress measurement results of as-received and the stress-relieved samples.

After stress relief, commercially pure aluminum (Al > 99.7%) powders with average size of 25 μm were cold sprayed on the flat samples by employing Centerline SST Series P cold spray system. The sample surface was grit-blasted (before the cold spray) with aluminum oxide. Al coating was deposited with nitrogen as the propellant gas at the following processing settings: temperature of 350 °C, pressure of 250 psi and standoff distance of 12 mm. The coat displayed bond strength of 22 MPa, hardness of 34–37 HB, and density greater than 99.5%. Fig. 4 shows the flat samples before and after the coating. Fig. 5 shows the coat-substrate interface bond.

X-ray Diffraction method was performed to measure the residual stresses induced by the coating process. Tests were performed by Lambda Technologies and Milan University. X-ray diffraction residual stress measurements were made at the surface of the AZ31 after removing the aluminum coating by electropolishing, and at nominal depths of 10, 20, 70, 160, 260, and 400×10^{-3} mm. Measurements were made in the extrusion direction at the center of coated face with irradiated area of 5.1×5.1 mm. X-ray diffraction residual stress measurements were performed using a $\sin^2(\psi)$ technique, in accordance with SAE HS-784, employing the diffraction of Mn Kα radiation in Lambda Technologies and Cr Kα radiation in Milan University from the (203) planes of the HCP structure of the AZ31. The

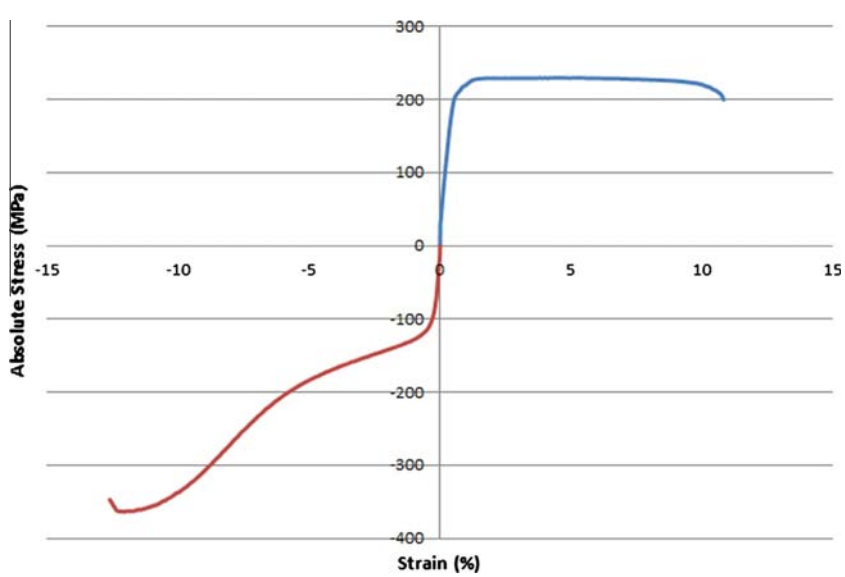

Fig. 3. Tension and compression behavior of AZ31B along extrusion direction (ED) [30].

Table 2
XRD stress measurement results on as-received and stress-relieved samples.

Sample/process	Lambda technologies		Milan polytechnic	
	Residual stress in extrusion direction (MPa)	Tolerance (MPa)	Residual stress in extrusion direction (MPa)	Tolerance (MPa)
As-received sample	−43	±1	−36.6	NA
Stress-relieved sample	2	±1	0	NA

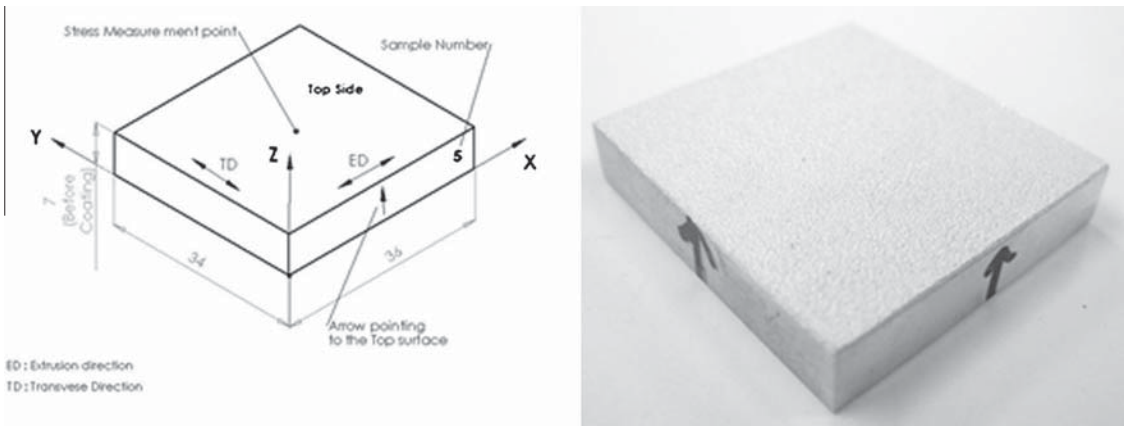

Fig. 4. Flat sample of AZ31B (a) uncoated sample and (b) coated Sample.

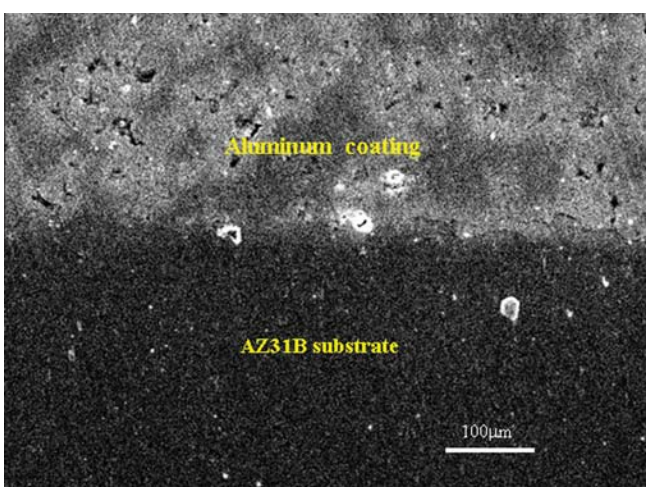

Fig. 5. Interface of aluminum coat and the AZ31B extrusion substrate.

samples were rocked through an angular range of ±1.5°. around the mean psi angles during the measurement to integrate the diffracted intensity over more grains and to minimize the influence of the grain size.

Material was removed electrolytically for subsurface measurements in order to minimize possible alteration of the subsurface residual stress distribution, as a result of material removal. All data obtained as a function of depth were corrected for the effects of the penetration of the radiation employed for residual stress measurement into the subsurface stress gradient.

The longitudinal residual stress distribution measured as a function of depth is shown in Fig. 6.

4. Residual stress modeling

The process of cold spray of aluminum particles on magnesium substrate was simulated using LSDYNA [32]. The focus of this simulation was the peening effect of the spraying, and the residual stress resulting from it. For simulation of the local deformation of AZ31B substrate due to collision of aluminum particles, the tension–compression plasticity material model (MAT_124) of LSDYNA is used. The MAT_124 material model allows for independent behavior in tension and compression, and hence captures the material asymmetry exhibited by magnesium extrusion. However, this material model is not accommodating material anisotropy and, therefore, the mechanical properties are assumed to be isotropic. Considering the dominant effect of asymmetry, when compared to directional anisotropy of magnesium extrusion in local plastic deformation, the latter assumption is justified. In MAT_124 the rate effect is modeled by the Cowper–Symonds strain rate model [32] using the following equation:

$$\frac{\sigma}{\sigma_0} = 1 + \left(\frac{\dot{\varepsilon}}{D}\right)^{\frac{1}{p}} \tag{1}$$

where $\dot{\varepsilon} = \sqrt{\dot{\varepsilon}_{ij}\dot{\varepsilon}_{ij}}$ is strain rate, σ is the Von Mises stress, σ_0 is the semi-static yield stress and D and p are the strain rate parameters. Najafi and Rais-Rohani [33] obtained AZ31B stress–strain curves in a wide strain rate range of 1 Hz to 1000 Hz. They found p = 3.09 and D = 24,124 Hz for AZ31B.

The tension and compression curves of AZ31B shown in Fig. 2, and other alloy parameters including density (1770 kg/m^3), Young's modulus (45 GPa), and Poisson's ratio (0.35), are used in the simulation. To introduce aluminum particles properties to LS-DYNA, the Johnson–Cook material model (MAT_15) is employed which is suitable for problems with a high rate of strain with proper material softening due to adiabatic temperature increase. In this material model, effects of strain, strain rate and temperature on yield strength are taken into account according to the following equation:

$$\sigma_y = \left(A + B\bar{\varepsilon}^{p^n}\right)\left(1 + C\ln\dot{\varepsilon}^*\right)\left(1 - T^{*^m}\right) \tag{2}$$

where A, B, C, n and m are material constants. $\dot{\varepsilon}^p$ is the effective plastic strain and $\dot{\varepsilon}^* = \frac{\dot{\varepsilon}^p}{\dot{\varepsilon}_0}$ is the ratio of effective plastic strain rate to

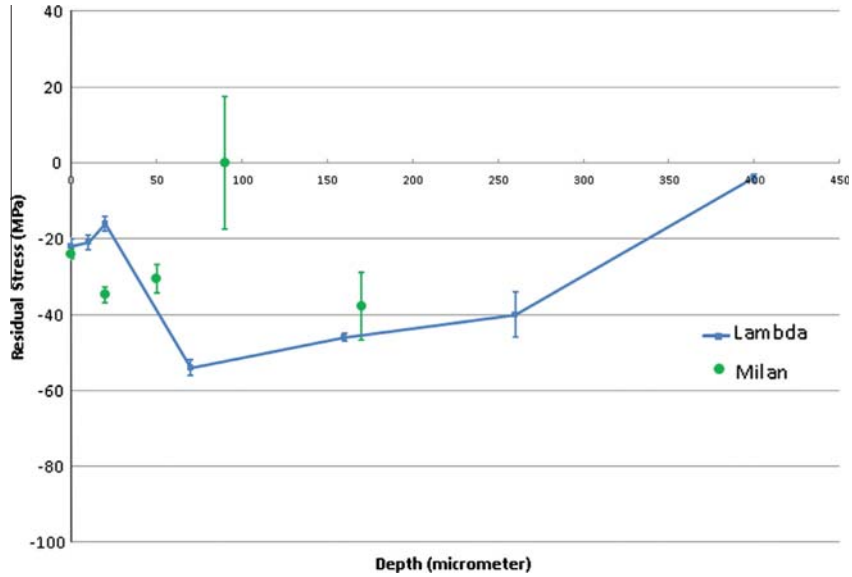

Fig. 6. Residual stress XRD measurement at surface and depth along extrusion direction.

strain rate at semi-static threshold, $\dot{\varepsilon}_0$. In Eq. (2), T^* is the impact of temperature defined by:

$$T^* = \frac{T - T_{room}}{T_{melt} - T_{room}} \tag{3}$$

where T is the instantaneous temperature, T_{room} is the room temperature and T_{melt} is the melting point of the material. Pierazzo et al. [34] extracted material model parameters of Johnson–Cook for AL-1100 by using the test data of Benck et al. [35]. These parameters are given in Table 3.

For the dissemination of stress waves due to high velocity collision of particles to the work piece, the following Gruneisen equation is used:

$$p = \frac{\rho_0 C_0^2 \mu \left[1 + \left(1 - \frac{\gamma_0}{2}\right)\mu - \frac{a}{2}\mu^2\right]}{\left[1 - (S_1 - 1)\mu - S_2 \frac{\mu^2}{\mu+1} - S_3 \frac{\mu^3}{(\mu+1)^2}\right]^2} + (\gamma_0 + d\mu)E; \quad \mu = \frac{\rho}{\rho_0} - 1 \tag{4}$$

where C_0 is the bulk speed of sound, ρ_0 is the initial density, ρ is the current density, S_1, S_2 and S_3 are the coefficients of the slope of the $U_s - U_p$ curve, U_s is the shock wave velocity, U_p is the particle velocity, γ_o is Gruneisen's gamma at the reference state, d is the first order correction coefficient per volume for γ_o and E is the internal energy per unit reference volume. Proper parameters of Gruneisen equation for Al 1100-O have been published by Group GMX-6, Los Alamos [36] (see Table 4).

Other material constants of AL 1100-O particles that are used here are density (2710 kg/m^3), Young's modulus (70 GPa), Poisson's ratio (0.33), shear modulus (26 GPa), and specific heat capacity (890 J/kg K).

Table 3
Johnson–Cook parameters for AL 1100-O [34,35].

Parameter	Value
A (MPa)	49
B (MPa)	157
n	0.167
C	0.016
m	1.7
T_{room} (K)	293
T_{melt} (K)	933

Table 4
Gruneisen equation of state parameters for AL 1100-O [36].

Parameter	Value
C_0 (m/s)	5328
S_1	1.338
S_2	0
S_3	0
γ_0	2
a	0

To determine the proper number of finite elements for simulation of AZ31B work piece, a convergence study was considered in which 8-node hexagonal elements were used with 6 degree-of-freedom per node.

Two different cases were modeled, the impact of a single particle, and random impact of multiple particles. The latter includes particles with same diameters, random diameters, and random shapes. In all of the cases, node to surface contact with a penalty formulation, and friction coefficient of 0.1 was considered. Modeling was verified by comparing the residual stress predicted by models with those measured experimentally by X-ray diffraction method. Finally, a parametric study was performed to study the sensitivity of residual stress to particle speed, size, shape, impact angle, and friction.

4.1. Impact of single particle

Impact of a single particle with a diameter of 40 μm with a flat AZ31B substrate of sizes 400 μm × 400 μm × 280 μm at velocity of 400 m/s has been simulated. An impact area of 120 μm × 120 μm × 100 μm has been discretized into a fine mesh with elements sizes of 4 μm × 4 μm × 4 μm. All displacements at the bottom of the work piece are fixed. The non-reflecting boundary has been used in the boundaries of the model in order to damp the wave fluctuations. Fig. 7 shows the developed finite element model. Since the velocity of impact is very high and the deformations are very large, the hourglass control with viscous form is used [32].

4.2. Random impact of multiple particles

In the real process, collision of particles to the substrate is random. For the simulation, 40 particles with equal diameter (D = 40 μm) have been considered. The work piece sizes in this

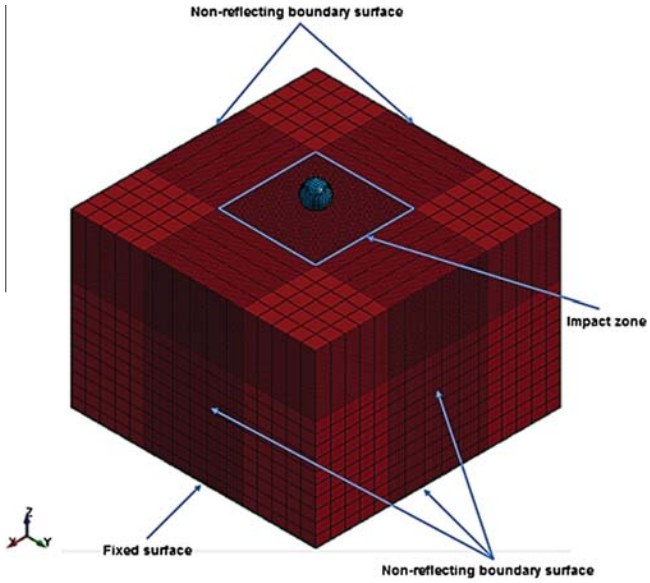

Fig. 7. Mesh configuration and developed finite element model.

model are 400 μm × 400 μm × 480 μm and the particles velocity is 400 m/s. The impact of the particles to each other is neglected. An isometric view of the model is depicted in Fig. 8.

To have a more realistic model, the sizes of the aluminum particle were also taken to be random. In result of this, in the third model, 10% of the entire particles (4 particles) are modeled with 20–38 μm diameter, 80% (32 particles) with 38–42 μm diameter and 10% with 42–60 μm diameter. An isometric view of the modeling is shown in Fig. 9.

A further model takes the particles shapes into account by considering them to be ellipsoidal rather than spherical. Therefore, the shape of the particles has been considered as an ellipsis with radii of a and b, and a/b ratio in the range of 0.5 to 2 has been assigned to each particle. In addition, the mass of each particle is the same and is equivalent to the mass of a AL 1100-O particle with diameter of 40 μm. An isometric view of this model is displayed in Fig. 10.

4.3. Model verification

In this section, results of the three simulations are compared with the XRD results (Fig. 11). In all simulated models, the residual stress through the depth is obtained at the center.

Results of the first model show a good agreement with the XRD tests for depth greater than 100 μm (Fig. 11). However, for the compressive residual stress on the surface, the discrepancy is considerable. The differences between the real conditions and the simulations assumptions can be accounted for this disagreement. Predictions of the second model, in which the size of particles is variable, show better results with respect to the first model when compared to experimental results. For example, the surface residual stress is closer to the measured value. Evaluation of effects of particle size on the simulation results shows that, when the particles size increases from 20 μm to 40 μm, the surface residual stress grows. However, the results show that the increase in surface residual stress for particle diameters in the range of 40–60 μm is negligible. Results of the third case represent the best estimation for surface residual stress (about 27% difference with the average experiment result). The study of effects of particle size shows that when a/b ratio is changed from 1 to 0.5 or from 1 to 2, the surface residual stress decreases considerably.

4.4. Parametric study

One of the effects of the cold spray coating process is to hamper the initiation and propagation of surface cracks by producing compressive residual stress on the surface. The level to which crack growth is postponed directly depends on the size and depth of the compressive residual stress profile. Fig. 12 shows a typical residual stress distribution induced in cold spray. The figure shows the main characteristics of this distribution and its important parameters: maximum compressive residual stress (σ_{rcmax}), surface residual stress (σ_{rs}), maximum tensile residual stress (σ_{rtmax}), depth of maximum tensile residual stress (d_p) and beneficial depth or depth of maximum compressive residual stress (d_b).

Alteration of each parameter has a direct impact on the efficiency of the process in terms of fatigue life enhancement. Therefore, to study the effects of parameters of the process on the residual stress profile and obtaining the optimum parameters for the process, it is necessary to examine the impact of each parameter on the process. In general, higher values for parameters like σ_{rs}, σ_{rcmax}, and d_p and lower values for parameters like d_b, σ_{rtmax} and d_{rtmax} are desirable. However, the single most important parameter is σ_{rs}. To examine the sensitivity of the residual stress to the main cold spray parameters (particle velocity, size, shape, incident angle and friction), a parametric study has been conducted. The range for parameters considered in the study is shown in Table 5.

The effect of particle velocity on residual stress is depicted in Fig. 13. The maximum compressive and tensile residual stresses

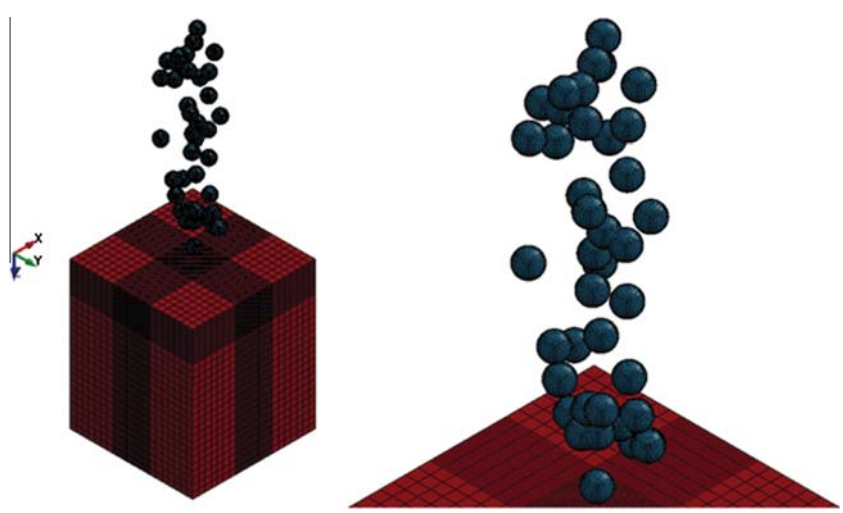

Fig. 8. Isometric view of multiple particles impact with same diameters of 40 μm.

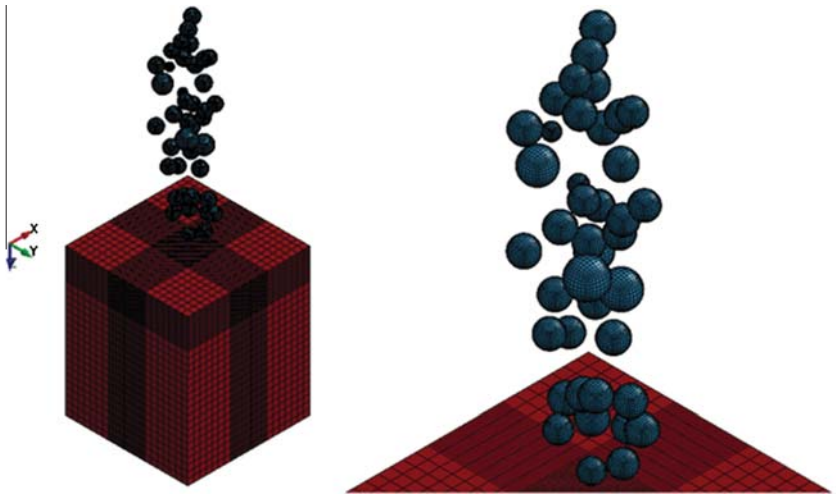

Fig. 9. Isometric view of random impact of multiple particles with different diameters.

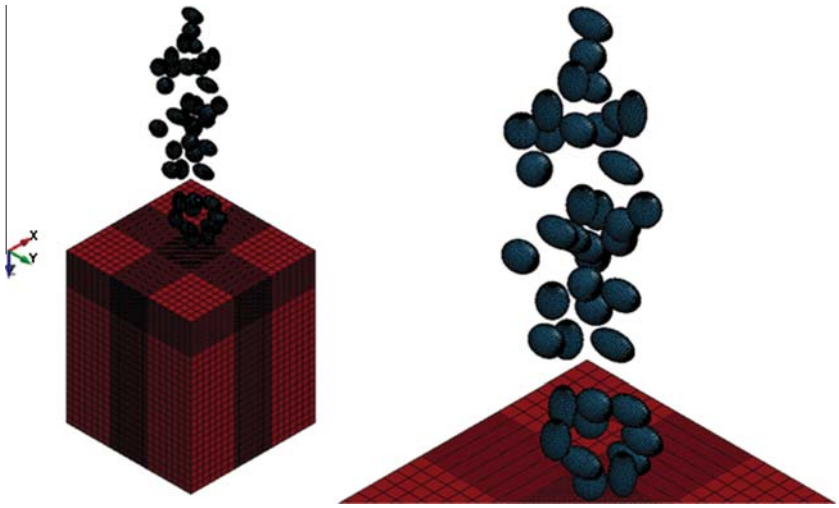

Fig. 10. Isometric view of random impact of multiple particles with different shapes and same masses.

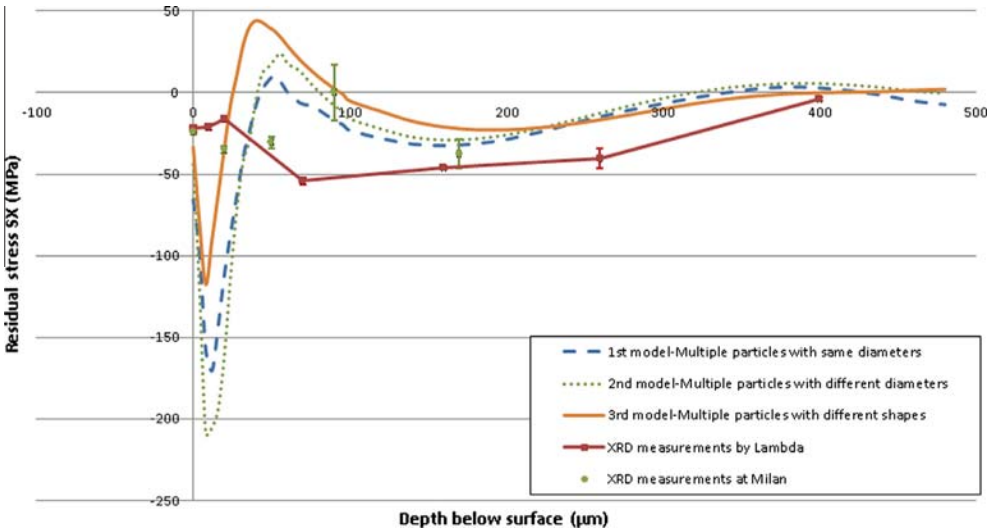

Fig. 11. Experiments against evaluated residual stress profile.

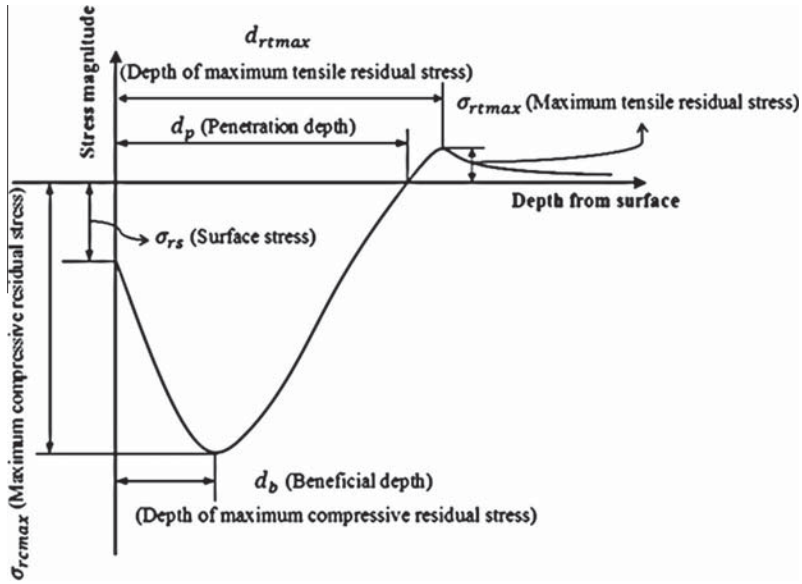

Fig. 12. Typical profile of residual stress induced by cold spray coating on a workpiece surface with its important characteristics [37].

Table 5
Selected parameters and their corresponding range for parametric study.

Parameters	Selected values
Particle velocity (m/s)	400, 500, 600, 700, 800, 900
Particle diameter (μm)	20, 30, 40, 50, 60
Particle shape (a/b)	0.25, 0.5, 1, 2, 4
Impact angle (°)	15, 30, 45, 60, 75, 90
Friction	0.1, 0.3, 0.5, 0.7, 1

are increased by increasing the particle velocity. Increase in particle velocity causes increase in kinetic energy of the particle which in turn partially converts to plastic energy required for the local deformation. Therefore, higher kinetic energy causes larger plastic region and larger residual stress in the workpiece. Furthermore, an increase in particle velocity results in larger d_b, d_{rtmax} and d_p in an approximately linear trend. Table 6 comprises values and changes of surface residual stress (σ_{rs}), maximum compressive residual stress (σ_{rcmax}), maximum tensile residual stress (σ_{rtmax}) and depth of maximum tensile residual stress (d_{rtmax}) due to change in particle velocity. The table data shows that the rate of change between consecutive values of σ_{rcmax} linearly increases, while the upward trend of σ_{rtmax} is nonlinear. Furthermore, with the increase of speed, the value of σ_{rs} moves toward to the positive values and hits a peak of 10.76 MPa, at speed of 700 m/s and, after that, declines as the speed increases.

Fig. 14 shows the residual stress curves for AZ31B with different particle sizes at a constant speed of 400 m/s. Parameters like σ_{rcmax}, σ_{rtmax}, d_b, d_p and d_{rtmax} increase when the particle velocity increases. These augmentations in the parameters are due to particle size, increase in mass and, consequently, increase in kinetic energy. Hence, impact of the particle to substrate transfers more energy to the workpiece and, in result, the plastic region becomes larger and deeper. Table 7 shows the residual stress distribution parameter changes with respect to particle size. The beneficial depth (d_b) linearly increases as the particles diameter is increased. A 10 μm increase in particle diameter causes d_b to be increased by 4 μm. In addition, Table 7shows a linear relation between σ_{rcmax} and

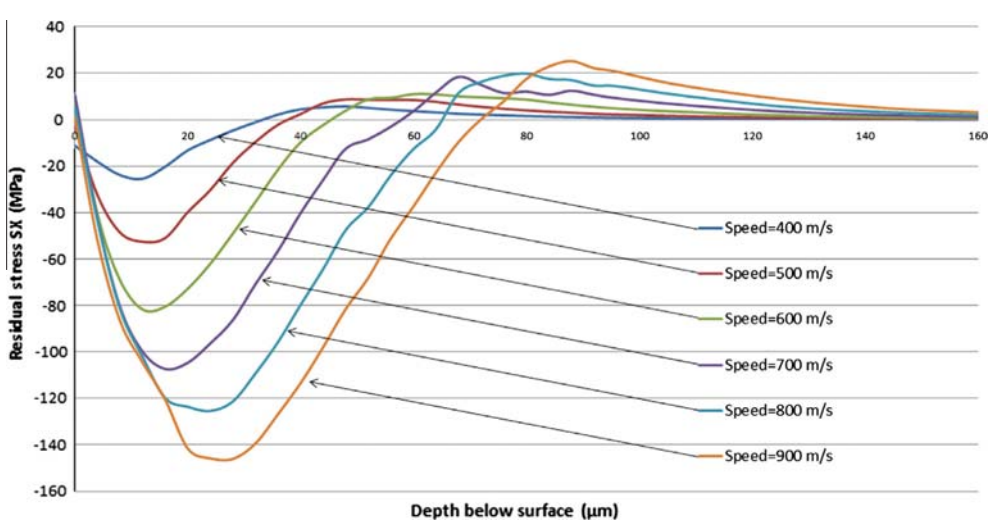

Fig. 13. Residual stress profile generated in an AZ31B substrate when impacted at different speeds by an Al 1100-O particle of 40 μm diameter.

Table 6
Effect of particle speed on σ_{rs}, σ_{rcmax}, σ_{rtmax} and d_{rtmax}.

Particle speed (m/s)	σ_{rs} (MPa)	Change in σ_{rs} (%)	σ_{rcmax} (MPa)	Increase in σ_{rcmax} (%)	σ_{rtmax} (MPa)	Increase in σ_{rtmax} (%)	d_{rtmax} (μm)	Increase in d_{rtmax} (%)
400	−11.18	–	−25.4	–	5.75	–	48	–
500	−3.04	−72.81	−52.52	106.77	8.77	52.52	50	4.17
600	8.12	−367.11	−81.72	55.6	11.02	25.66	60	20
700	10.76	−32.51	−107.32	31.33	18.46	67.51	68	13.33
800	5.48	49.07	−125.42	16.87	19.89	7.75	80	17.65
900	0.68	87.59	−146.09	16.48	25.24	26.9	88	10

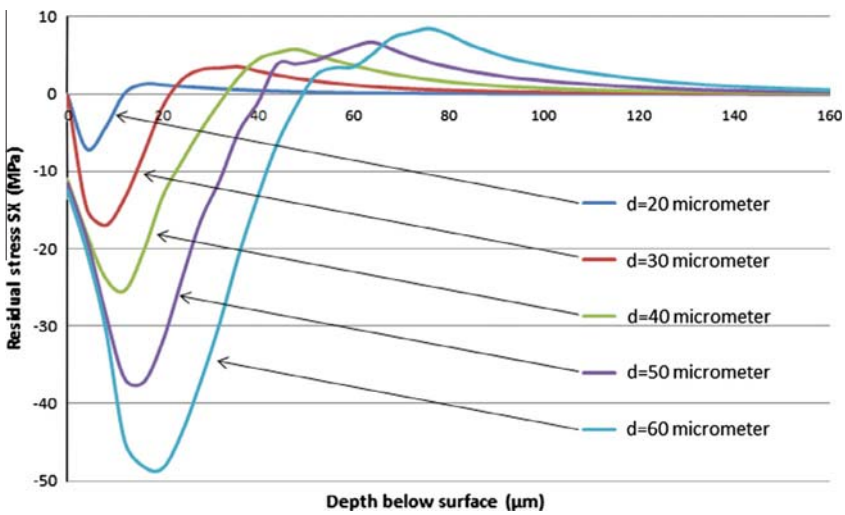

Fig. 14. Residual stress profile generated in an AZ31B substrate at constant particle velocity of 400 m/s with different particle diameters.

particle size. Moreover, the surface residual stress (σ_{rs}) shows a significant change at particle size of 40 μm and no appreciable change after that for larger particles.

To study the effect of shape, an ellipsoidal shape with varying aspect ratio (a/b) was considered as is shown in Fig. 14. Fig. 15 denotes the effects of various a/b ratios on residual stress curve. The figure shows that, from $a/b = 1$ onwards, penetration depth (d_p) and beneficial depth (d_b) remain unchanged while increase in a/b causes increase in maximum compressive residual stress (σ_{rcmax}). Increase in σ_{rcmax} is due to increase in a/b which causes the particle to become wider and likewise the contact surface between particles and substrate increases. Table 8 shows the values and percentages of increase in surface residual stress (σ_{rs}), maximum compressive residual stress (σ_{rcmax}), maximum tensile residual stress (σ_{rtmax}) and depth of maximum tensile residual stress (d_{rtmax}) as the a/b ratio increases. It can be concluded that as the material

Table 7
Effect of particle size on σ_{rs}, σ_{rcmax}, σ_{rtmax} and d_{rtmax}.

Particle diameter (μm)	σ_{rs} (MPa)	Increase in σ_{rs} (%)	σ_{rcmax} (MPa)	Increase in σ_{rcmax} (%)	σ_{rtmax} (MPa)	Increase in σ_{rtmax} (%)	d_{rtmax} (μm)	Increase in d_{rtmax} (%)
20	−0.2	–	−7.1	–	1.26	–	16	–
30	−0.29	45	−16.98	139.15	3.51	178.57	36	125
40	−11.18	3755.17	−25.4	49.59	5.75	63.82	48	33.33
50	−11.56	3.4	−37.22	46.54	6.68	16.17	64	33.33
60	−12.53	8.39	−48.34	29.88	8.44	26.35	76	18.75

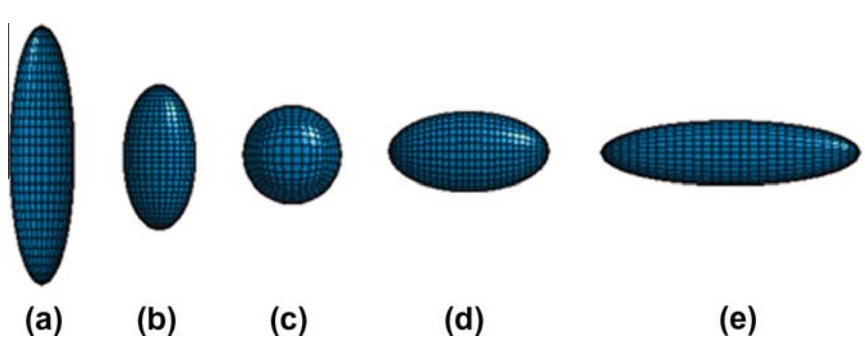

Fig. 15. Shapes of particles with different aspect ratio: (a) $a/b = 0.25$, (b) $a/b = 0.5$, (c) $a/b = 1$, (d) $a/b = 2$ and (e) $a/b = 4$.

Table 8
Effect of particle shape on σ_{rs}, σ_{rcmax}, σ_{rtmax} and d_{rtmax}.

Aspect ratio of particle (a/b)	σ_{rs} (MPa)	Changes in σ_{rs} (%)	σ_{rcmax} (MPa)	Increase in σ_{rcmax} (%)	σ_{rtmax} (MPa)	Increase in σ_{rtmax} (%)	d_{rtmax} (μm)	Increase in d_{rtmax} (%)
0.25	−1.32	–	−5.76	–	2.02	–	20	–
0.5	−4.42	234.85	−9.23	60.24	2.2	8.91	28	40
1	−11.18	152.94	−25.4	175.19	5.75	161.36	48	71.43
2	1.41	−112.61	−36.68	44.41	7.41	28.87	48	0
4	5.79	−310.64	−58.09	58.37	10.51	41.84	48	0

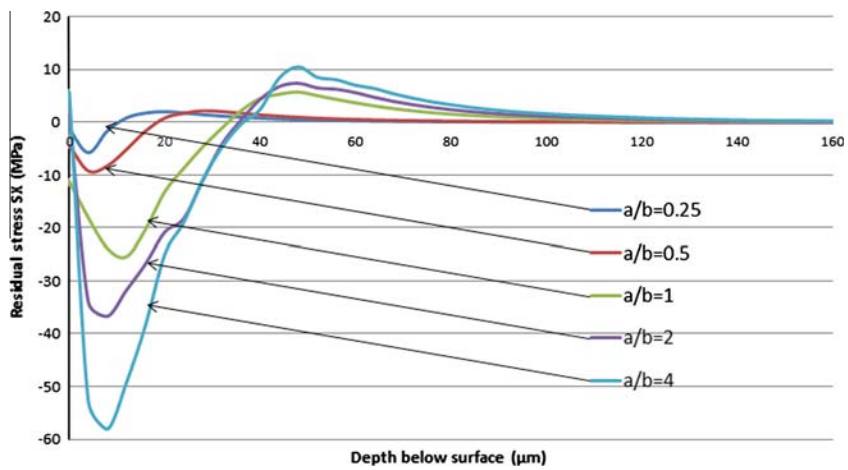

Fig. 16. Residual stress profile generated in an AZ31B substrate when impacted at 400 m/s by Al 1100-O particle with different shapes (aspect ratio) and same mass.

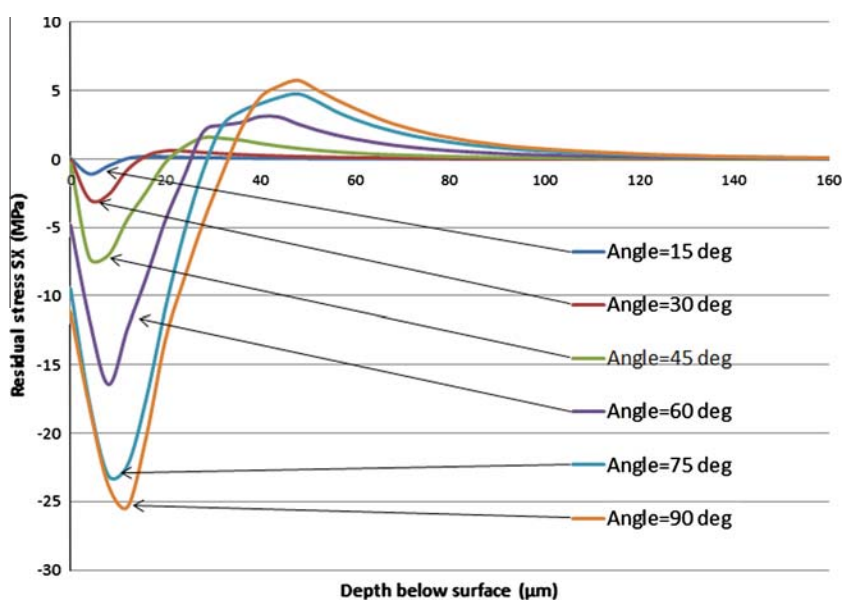

Fig. 17. Residual stress profile generated in an AZ31B substrate when impacted at 400 m/s by an Al 1100-O particle with 40 μm diameter at different impact angles.

shape changes from sharp to spherical, the compressive residual stress on the surface increases. When the particle shape passes the spherical shape and becomes tauter, tensile stress spreads over larger number of surface elements and accordingly the average of surface residual stress becomes tensile (positive) and rises as the a/b increases (see Fig. 16).

The impact angle of the particle with the substrate depends on the type of cold spray machine, type of nozzle, exit conditions of particles from the nozzle, and substrate surface condition. Oblique collision of particles when the cold spray gun is at the right angle with the substrate may be due to two reasons: (1) angular exit of particles from the nozzle, and (2) roughness of the workpiece surface. Residual stress distribution for different incident angles is displayed in Fig. 17. An increase in impact angle from 15° to 90° results in higher values of σ_{rcmax}, σ_{rtmax}, σ_{rs} and d_{rtmax}. On the one hand, when the particle impacts the substrate with an angle less than 90°, the particle can slide better on the surface and the friction between particle and surface increases which in turn causes the increase in temperature of the particle. Therefore, less energy is transferred to the workpiece and consequently more tensile force

Table 9
Effect of impact angle on σ_{rs}, σ_{rcmax}, σ_{rtmax} and d_{rtmax}.

Impact angle (°)	σ_{rs} (MPa)	Changes in σ_{rs} (%)	σ_{rcmax} (MPa)	Increase in σ_{rcmax} (%)	σ_{rtmax} (MPa)	Increase in σ_{rtmax} (%)	d_{rtmax} (μm)	Increase in d_{rtmax} (%)
15	0.03	–	−1.09	–	0.19	–	16	–
30	0.02	33.33	−2.95	170.64	0.6	215.79	20	25
45	−0.3	1600	−7.24	145.42	1.57	161.67	28	40
60	−4.84	1513.33	−16.44	127.07	3.11	98.09	40	42.86
75	−9.48	95.87	−23.12	40.63	4.77	53.38	48	20
90	−11.18	17.93	−25.4	9.86	5.75	20.55	48	0

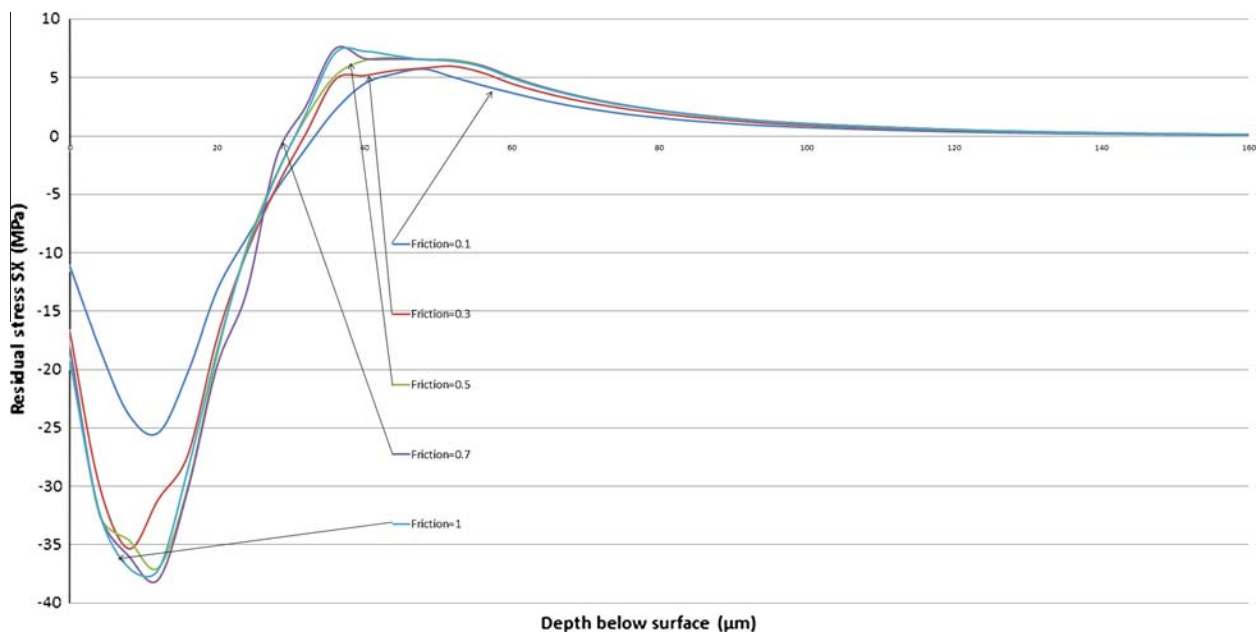

Fig. 18. Residual stress profile generated in an AZ31B substrate when impacted at 400 m/s by an Al 1100-O particle of 40 μm diameter with different friction coefficients.

Table 10
Effect of friction coefficient on σ_{rs}, σ_{rcmax}, σ_{rtmax} and d_{rtmax}.

Friction coefficient	σ_{rs} (MPa)	Increase in σ_{rs} (%)	σ_{rcmax} (MPa)	Increase in σ_{rcmax} (%)	σ_{rtmax} (MPa)	Increase in σ_{rtmax} (%)	d_{rtmax} (μm)	Increase in d_{rtmax} (%)
0.1	−11.18	–	−25.4	–	5.75	–	48	–
0.3	−16.79	50.18	−35.34	39.13	5.98	4	48	0
0.5	−18.06	7.56	−36.99	4.67	6.72	12.37	44	−8.33
0.7	−18.23	0.94	−37.98	2.68	7.48	11.31	40	−9.09
1	−19.29	5.81	−37.15	−2.19	7.28	−2.67	40	0

is applied on the surface that decreases the surface compressive residual stress. Information regarding σ_{rcmax}, σ_{rtmax}, σ_{rs} and d_{rtmax} for impact angle is presented in Table 9. The table shows that parameters σ_{rcmax}, σ_{rtmax}, σ_{rs} and d_{rtmax} nonlinearly increase as impact angle increases.

To study the effects of particle/substrate friction on the process, friction coefficient was varied from 0.1 to 1. Fig. 18 demonstrates variation of the residual stress profile during the increase of the friction coefficient. Even though the change in friction from 0.1 to 0.3 has a substantial effect on the residual stress curve, changes after 0.3 are negligible. Results shown in Table 10 suggest that increase of friction coefficient does not considerably impact the values of d_b, d_p, σ_{rtmax} and d_{rtmax}.

5. Conclusions

The residual stress induced by cold spray coating of the aluminum powder on the magnesium alloy, AZ31B, was evaluated by both experimental and numerical methods. For experimental evaluation, residual stress on the surface of substrate and in the depth was measured using X-ray diffraction. The results were showing compressive residual stress on the surface to be in the range of −20 MPa that increased to −54 MPa compressive stress in the depth of about 70 μm and dissipated to zero at the depth of 400 μm. The residual stress did not transform to tensile stress in the depth of measurement that shows this transformation is happening beyond 400 μm.

Numerical evaluation of induced residual stress was performed using Explicit FEA package, LS-DYNA. Tension–compression plasticity material model (MAT_124), the closest material model of this software to the behavior of AZ31B, was employed for the simulation. To capture high strain rate of cold spray coating process, Cowper–Symonds model was used. For aluminum particles, Johnson–Cook material model (MAT_15) was used, which is suitable for simulating high strain rate problems and also the problems in which adiabatic heat transfer and material softening occurs. These characteristics are needed for simulating the high velocity

impact and plastic deformation of the particles in the cold spray coating. Four main models were developed using single and multiple particles models. Single particle models were used for parametric study and multiple particle models were employed for comparing to the XRD measurements. To better mimic the cold spray condition, three multiple material models including random arrangement of particles with identical spherical particles, different size spherical particles, and different ellipsoid shape particles were developed.

Parametric study performed on the single particle model to evaluate the effect of velocity, diameter, shape, and angle of impact of particles, as well as the friction between particles and substrate, on the induced residual stresses. Following conclusions may be drawn from the parametric study.

- With the increase in particle speed, maximum compressive residual stress (σ_{rcmax}) and depth of maximum tensile residual stress (d_{rtmax}) increase in a uniform and linear manner, while maximum tensile residual stress (σ_{rtmax}) increases nonlinearly. In addition, surface residual stress (σ_{rs}) increases in a positive way (tensile) with the speed increase up to 700 m/s and afterward decreases with the increased velocity. Moreover, the results show that beneficial depth (d_b) and penetration depth (d_p) increase linearly with the increase in speed.
- With particle size increase to the diameter of 30 μm, surface residual stress (σ_{rs}) slightly increases and then with the increase in particle size from 30 μm to 40 μm, the σ_{rs} increases significantly. Thereafter, σ_{rs} remains unchanged. Furthermore, other parameters σ_{rcmax}, σ_{rtmax}, d_{rtmax}, d_b and d_p increase with the increase in particle speed.
- Increase in impact angle causes σ_{rs}, σ_{rcmax}, σ_{rtmax} and d_{rtmax} parameters to increase nonlinearly, while d_b is unaffected by the increase of the impact angle.
- With increase in friction coefficient between particle and workpiece, parameters like d_b, d_p, σ_{rtmax} and d_{rtmax} remain unchanged. Also, σ_{rs} and σ_{rcmax} increase when the friction coefficient is between 0.1 to 0.3 but remain unchanged after 0.3.

Acknowledgements

The authors would like to acknowledge the financial support of The Initiative for Automotive Manufacturing Innovation (IAMI) of Canada and the participation of CenterLine Windsor Ltd.

References

[1] Tari DG, Worswick MJ, Experimental investigation of anisotropy evolution of AZ31 magnesium alloy sheets under tensile loading, in ESAFORM, 2011. p. 1547–52.
[2] Chen X, Wu SR, Wagner DA, Hu W. Study of die cast magnesium components for crash safety. IJ Crash 2002:429–40.
[3] Logan S, Kizyma A, Patterson C, Rama S. Lightweight magnesium intensive body structure. In: SAE world congress, Detroit, 2006.
[4] Papyrin A, Kosarev V, Klinkov S, Alkhimov A, Fomin V. Cold spray technology. Elsevier; 2006.
[5] Magensium alloys from corrosion. <http://www.thefabricator.com>; 2012 [retrieved on 05.07.12.
[6] Carpinteri A, Brighenti R, Vantadori S. Influence of the cold-drawing process on fatigue crack growth of a V-notched round bar. Int J Fatigue 2010;32(7):1136–45.
[7] Price TS, Shipway PH, McCartney DG. Effect of cold spray deposition of a titanium coating on fatigue behaviour of a titanium alloy. J Therm Spray Technol 2006;15:507–12.
[8] Cizek J, Kovarik O, Siegl J, Khor KA, Dlouhy I. Influence of plasma and cold spray deposited Ti layers on high cycle fatigue properties of Ti6Al4V substrates. Surf Coat Technol 2013;217:23.
[9] Luzin V, Spencer K, Zhang MX. Residual stress and thermo-mechanical properties of cold spray metal coatings. Acta Mater 2001;59:1259–70.
[10] Tsui YC, Clyne TW. An analytical model for predicting residual stresses in progressively deposited coatings Part 1: planar geometry. Thin Solid Films 1997;306:23–33.
[11] Spencer K, Luzin V, Matthews N, Zhang MX. Residual stresses in cold spray Al coatings: the effect of alloying and of process parameters. Surf Coat Technol 2012;206:4249–55.
[12] Sansoucy E, Kim GE, Moran AL, Jodoin B. Mechanical characteristics of Al–Co–Ce coatings produced by the cold spray process. J Therm Spray Technol 2007;16:651–60.
[13] Jeong CY, Ha S. Fatigue properties of Al–Si casting alloy with cold sprayed Al/SiC coating. Int J Cast Met Res 2008;21:235–8.
[14] Ghelichi R, MacDonald D, Bagherifard S, Jahed H, Guagliano M, Jodoin B. Microstructure and fatigue behaviour of cold spray coated Al5052. Acta Mater 2012;60:6555–61.
[15] Moridi M, Hassani-Gangaraj SM, Guagliano M, Vezzu S. Effect of cold spray deposition of similar material on fatigue behaviour of AL 6082 alloy. In: Carroll J, editor. Conference proceedings of the society for experimental mechanics series. Fracture and fatigue, proceedings of the 2013 annual conference on experimental and applied mechanics, vol. 7. The Society for Experimental Mechanics, Inc.; 2014. p. 51–7.
[16] Assadi H, Gartner F, Stoltenhoff T, Kreye H. Bonding mechanism in cold gas spraying. Acta Mater 2003;51:4379–94.
[17] Grujicic M, Saylor JR, Beasley DE, DeRosset WS, Helfritch D. Computational analysis of the interfacial bonding between feed-powder particles and the substrate in the cold-gas dynamic-spray process. Appl Surf Sci 2003;219:211–27.
[18] Li Wen-Ya, Liao Hanlin, Li Chang-Jiu, Bang Hee-Seon, Coddet C. Numerical simulation of deformation behaviour of Al particles impacting on Al substrate and effect of surface oxide films on interfacial bonding in cold spraying. Appl Surf Sci 2007;253:5084–91.
[19] Kumar S, Bae Gyuyeol, Kang Kicheol, Yoon Sanghoon, Lee Changhee. Effect of powder state on the deposition behaviour and coating development in kinetic spray process. J Phys D Appl Phys 2009;42:075305.
[20] Li Wen-Ya, Gao Wei. Some aspects on 3D numerical modeling of high velocity impact of particles in cold spraying by explicit finite element analysis. Appl Surf Sci 2009;255:7878–92.
[21] Li Wen-Ya, Yin Shuo, Wang Xiao-Fang. Numerical investigations of the effect of oblique impact on particle deformation in cold spraying by the SPH method. Appl Surf Sci 2010;256:3725–34.
[22] Ghelichi R, Bagherifard S, Guagliano M, Verani M. Numerical simulation of cold spray coating. Surf Coat Technol 2011;205:5294–301.
[23] Raletz F, Vardelle M, Ezo'o G. Critical particle velocity under cold spray conditions. Surf Coat Technol 2006;201:1942–7.
[24] Yin Shuo, Wang Xiaofang, Li Wenya, Liao Hanlin, Jie Hongen. Deformation behaviour of the oxide film on the surface of cold sprayed powder particle. Appl Surf Sci 2012;259:294–300.
[25] Xie Jing, Nelias Daniel, Walter-Le Berre Helene, Ito Kiyohiro, Ichikawa Yuji, Ogawa Kazuhiro. Numerical modeling for cold sprayed particle deposition. In: 40th Leeds-Lyon symposium on tribology & tribochemistry; 2013.
[26] Yin Shuo, Zhang Meng, Guo Zhiwei, Liao Hanlin, Wang Xiaofang. Numerical investigations on the effect of total pressure and nozzle divergent length on the flow character and particle impact velocity in cold spraying. Surf Coat Technol 2013;232:290–7.
[27] Ghelichi R, Bagherifard S, MacDonald D, Fernandez-Pariente I, Jodoin B, Guagliano M. Experimental and numerical study of residual stress evolution in cold spray coating. Appl Surf Sci 2013;288:26–33.
[28] Mahmoudi H, Jahed H, Villafuerte J. The effect of residual stress induced by cold spray coating on fatigue life of magnesium alloy AZ31B, magnesium 2012, Vancouver, Canada, 2012.
[29] Albinmousa J, Jahed H, Lambert S. Cyclic behaviour of wrought magnesium alloy under multiaxial load. Int J Fatigue 2011;33(8):1127–39.
[30] Albinmousa J, Jahed H, Lambert S. Cyclic axial and cyclic torsional behaviour of extruded AZ31B magnesium alloy. Int J Fatigue 2011;33(8):1127–39.
[31] ASM metals handbook, vol. 2, 9th ed., 1989.
[32] LS-DYNA3D. User's Manual. Ver. 950. Livermore software technology corporation, Livermore, California, 1999.
[33] Najafi A, Rais-Rohani M. Mechanics of axial plastic collapse in multi-cell, multi-corner crush tubes. Thin-Wall Struct 2011:1–12.
[34] Pierazzo E, Artemieva N, Asphaug E, Baldwin EC, Cazamias J, Coker R, et al. Validation of numerical codes for impact and explosion cratering: impacts on strength and metal targets. Meteorit Planet Sci 2008:1917–38.
[35] Benck RF, Filbey Jr GL, Murray Jr EA. Quasi-static compression stress-strain curves-IV, 2024–T3510 and 6061-T6 aluminum alloys. In: BRL Memorandum Report 2655, USA Ballistic Research Laboratories, Maryland, 1976.
[36] "Selected Hugoniots", Group GMX-6, Los Alamos Scientific Lab., LA-4167-MS, 1969.
[37] Shivpuri Rajiv, Cheng Xiaomin, Mao Yongning. Elasto–plastic pseudo-dynamic numerical model for the design of shot peening process parameters. Mater Des 2009;30:3112–20.